Geophysical Monitoring of Hydrological and Biogeochemical Transformations Associated with Cr(VI) Bioremediation

SUSAN S. HUBBARD,*,† KEN WILLIAMS,†
MARK E. CONRAD,†
BORIS FAYBISHENKO,† JOHN PETERSON,†
JINSONG CHEN,† PHIL LONG,‡ AND
TERRY HAZEN†

Earth Science Division, 1 Cyclotron Rd MS 90-1116, Lawrence Berkeley National Laboratory, Berkeley, CA 94720, and Pacific Northwest Laboratories, Richland, WA

Understanding how hydrological and biogeochemical properties change over space and time in response to remedial treatments is hindered by our ability to monitor these processes with sufficient resolution and over field relevant scales. Here, we explored the use of geophysical approaches for monitoring the spatiotemporal distribution of hydrological and biogeochemical transformations associated with a Cr(VI) bioremediation experiment performed at Hanford, WA. We first integrated hydrological wellbore and geophysical tomographic data sets to estimate hydrological zonation at the study site. Using results from laboratory biogeophysical experiments and constraints provided by field geochemical data sets, we then interpreted time-lapse seismic and radar tomographic data sets, collected during thirteen acquisition campaigns over a three year experimental period, in terms of hydrological and biogeochemical transformations. The geophysical monitoring data sets were used to infer: the spatial distribution of injected electron donor; the evolution of gas bubbles; variations in total dissolved solids (nitrate and sulfate) as a function of pumping activity; the formation of precipitates and dissolution of calcites; and concomitant changes in porosity. Although qualitative in nature, the integrated interpretation illustrates how geophysical techniques have the potential to provide a wealth of information about coupled hydrobiogeochemical responses to remedial treatments in high spatial resolution and in a minimally invasive manner. Particularly novel aspects of our study include the use of multiple lines of evidence to constrain the interpretation of a long-term, field-scale geophysical monitoring data set and the interpretation of the transformations as a function of hydrological heterogeneity and pumping activity.

1. Introduction and Background

The objective of this study was to explore the use of geophysical approaches for monitoring the spatiotemporal distribution of hydrological and biogeochemical transformations associated with a Cr(VI) bioremediation experiment.

Our study was motivated by the hypothesis that several of the expected transformations would yield end products that could be detectable using time-lapse geophysical methods. Recent studies have demonstrated how indirect (yet spatially extensive) geophysical data sets can be integrated with direct (yet sparse) hydrological data to provide estimates of subsurface properties in high resolution and in a minimally invasive manner. Two recent books (*1, 2*) describe the state-of-the-art in this field of hydrogeophysics. Although hydrogeophysical challenges exist (e.g., ref *3*), recent synthetic and field studies have illustrated how geophysically obtained hydrological property estimates have improved the prediction of contaminant transport in natural systems over predictions based only on wellbore-based characterization data sets (*4, 5*).

Several recent studies have also explored the effects of microbial processes on geophysical attributes (*6, 7*). For the most part, these studies have been performed at the laboratory scale to investigate time-lapse changes in a geophysical attribute corresponding to a particular biogeochemical transformation. Although the studies hint at the potential that these methods have for field-scale monitoring, only a few studies have attempted to use geophysical methods at the field scale to monitor processes that occur in association with in situ contaminant remediation (e.g., ref *8*).

Here, we build upon these recent efforts by using multiple lines of evidence to aid in the interpretation of three-year, field-scale geophysical monitoring data set in terms of several hydrobiogeochemical transformations and in the presence of hydrogeological heterogeneity and variable pumping activity. Our study involved several components, including (a) laboratory-scale experiments designed to explore electrical, seismic, and radar responses to various biogeochemical transformations relevant to the Cr(VI) biostimulation; (b) analysis of geochemical data collected from field boreholes over the course of ~2 years; (c) estimation of hydraulic conductivity zonation using field geophysical and hydrological data sets; (d) acquisition and reduction of time-lapse, field-scale tomographic radar, and seismic data sets collected over the course of ~3 years; and (e) integrated interpretation of the field geophysical monitoring data sets in terms of hydrological and biogeochemical transformations, using information available from a–d.

1.1. The Hanford 100H Cr(VI) Bioremediation Experiment. Our geophysical monitoring study was performed as part of an effort to assess the ability to bioremediate the groundwater at the 100H area of the Department of Energy (DOE) Hanford Site, which is located ~1000 m from the Columbia River. The contaminant of concern at this site is hexavalent chromium (or chromate, Cr(VI)). Cr(VI) exists in strongly oxidizing environments and is very mobile and acutely toxic, while Cr(III) exists in moderately oxidizing and reducing environments and is immobile and not toxic. The pilot experiment was performed to evaluate the ability of an electron donor called hydrogen release compound (HRC) to stimulate biological activity, thereby creating a reducing environment that will cause the transformation of Cr(VI) to Cr(III). HRC is a viscous, denser than water ($\rho = 1.\text{g/cm}^3$), slow-release polylactate that is designed to remain near the injection region and to slowly release soluble and bioavailable lactic acid downgradient to stimulate sustained biological activity.

The bioremediation pilot experiment was performed in the saturated section of the Hanford formation within a small area of the 100H site. This formation is dominated by calcite-rich, unconsolidated, interfingered, high-permeability gravel

* Corresponding author phone: (510)-486-5266; fax (510)-486-5686; e-mail: sshubbard@lbl.gov.
† Lawrence Berkeley National Laboratory.
‡ Pacific Northwest Laboratories.

and sand layers. The water table is located within the Hanford formation at ~12.2 m, and the base of the Hanford formation is located at approximately 14.3 m. The Hanford formation rests atop the Ringold Formation, which at the 100H study site is dominated by low-permeability fine grained sediments.

Historical monitoring near the 100H study site indicated that Cr(VI) concentrations of up to ~160 ppb in the groundwater within the Hanford formation had persisted for over a decade, whereas recent measurements indicate a decrease in concentrations of 80–100 ppb. The 100H pilot study site was developed with the objective of reducing the concentrations within the saturated Hanford zone to below the U.S. Environmental Protection Agency's maximum contaminant level (MCL) for Cr(VI) of 10 ppb.

Development of the pilot study site was performed in 2004, including the installation of an injection well (Well 45) and a downgradient monitoring well (Well 44); the wellbore geometry and example wellbore lithology and construction are given in the Supporting Information. The biostimulation involved injection of 18.2 kg of HRC mixed with 10 g of ^{13}C-labeled lactate into Well 45. Pumping was initiated three times during the experiment. Two new wellbores (Wells 41 and 42) were drilled approximately two years poststimulation; one was located between the injection and monitoring wells, whereas the other was located ~5 m off of the study transect. Monitoring data showed that Cr(VI) concentrations dropped below water MCL within one month of the HRC injection, and concentrations remained below background concentration for at least two years after stimulation. A timeline of the HRC injection, pumping campaigns, and geophysical acquisition campaigns is given in the Supporting Information.

1.2. Geophysical Methods. We provide a very brief background of the different geophysical methods that were used for this study and discuss petrophysical relationships that link the geophysical attributes to hydrogeochemical properties.

1.2.1. Electrical Methods. Electrical methods involve the application of current and the measurement of voltages between electrodes. Perhaps the most common petrophysical relationship for near-subsurface geophysical exploration is Archie's Law (*9*). For saturated, porous geological materials, Archie's Law expresses the effective conductivity (σ_{eff}) as a function of porosity (**n**), the electrical conductivity of the pore water (σ_w), and the electrical conductivity associated with surface conduction (σ_{surface}):

$$\sigma_{\text{eff}} = \sigma_w n^m + \sigma_{\text{surface}} \tag{1}$$

where *m* is Archie's exponent. Equation 1 is commonly used with electrical conductivity measurements to estimate porosity or the electrical conductivity of pore fluids, which in turn is often expressed as a function of total dissolved solids (TDS) of aqueous solutions, using empirical relationships (*10*) such as

$$\sigma_w(S/m) \approx a \times \text{TDS(mg/L)} \tag{2}$$

where, depending upon the ionic composition and temperature of the solution, the constant *a* can range from ~1.2 × 10^{-4} to ~2.0 × 10^{-4}. Detailed information about electrical data acquisition, inversion techniques, and petrophysical relationships is available elsewhere (*11, 12*).

1.2.2. Radar Methods. Radar and time domain reflectometry (TDR) methods use electromagnetic energy in the 50 MHz to low GHz frequency range to probe geological materials. TDR methods involve propagating an electromagnetic signal along waveguides inserted into the material of interest, and measuring the velocity and amplitude of the traveling wave (*13*). Because of the small measurement volume associated with TDR probes, this method is commonly used for laboratory investigations. Tomographic radar

data acquisition consists of placing a transmitter and a receiver in separate boreholes and moving them successively until many transmitter and receiver locations have been occupied. The travel time of the direct arrival and associated amplitude information is extracted from the recorded waveforms, and inversion algorithms are used to transform this information into estimations of velocity and attenuation between the boreholes (*14*).

At the frequency of operation for TDR and radar systems, the separation (polarization) of opposite electric charges within a material subjected to an external electric field dominates the electrical response. The dielectric constant (*k*), which used to describe these high-frequency electrical properties, can be approximated from the velocity (*V*) of the radar signal (*15*) by

$$\kappa \approx \left(\frac{c}{V}\right)^2 \tag{3}$$

where *c* is the propagation velocity of electromagnetic waves in free space. The large contrast in dielectric constant between wet and dry materials renders radar and TDR methods very effective for providing information about water saturation.

Dielectric mixing models have been used to express the effective dielectric constant (κ_{eff}) of soils having a dielectric contribution from a variety of components (*16*), such as the expression for a three-component, soil–water–air system:

$$\kappa_{\text{eff}} = \left(Sn\kappa_w^\gamma + (1-n)\kappa_g^\gamma + n(1-S)\kappa_a^\gamma\right)^{\frac{1}{\gamma}} \tag{4}$$

In eq 4, *S* is water saturation; *n* is the soil porosity; κ_w, κ_g, and κ_a are the unitless dielectric constants of pore water, soil grains, and air, respectively; and γ is a factor that accounts for the orientation of the electrical field with respect to the geometry of the medium (which is commonly assumed to be 0.5 for an isotropic medium). Although idealistic, the mixing model shown in eq 4 can be useful for exploring changes in dielectric constant as a function of the type of pore fluid, mineralogy, and porosity.

Using high-frequency radar data and under the low-loss conditions, electrical conductivity can also be estimated with radar attributes following

$$\sigma[S/m] \approx \frac{\sqrt{\kappa}\alpha}{A} \tag{5}$$

where α is the attenuation coefficient in dB/m, and *A* (=1680 dB/S) is a constant that incorporates unit conversions and free-space impedance (*17*). Although approximate, eq 5 permits estimation of electrical conductivity using radar-derived attributes (e.g., refs *8, 17*). Similarly, the amplitude of the recorded TDR waveform can also be used to estimate electrical conductivity (*18*).

1.2.3. Seismic Methods. Seismic methods use sensitive geophones to measure disturbances that propagate outward from the source as a series of wavefronts. Field-based seismic tomographic data can be collected using the same concept described for tomographic radar methods, and the travel times and amplitudes can be inverted to obtain estimates of the distribution of seismic velocity and attenuation between the wellbores. A review of seismic method acquisition, processing, inversion, and interpretation for hydrological investigations is available elsewhere (*19*). Seismic velocity and attenuation are related to the bulk elastic properties of the sediment and pore fluids, which in turn depend on mineralogy, fluid chemistry, and intergranular structure (*20*).

2. Laboratory Experiments and Field Data Sets

In this section, we present the laboratory experimental results and the field geochemical, hydrological, and geophysical data sets that will be used in Section 3 to assist in the interpretation

TABLE 1. Summary of Geophysical Attribute Responses to System Transformations That Were Expected to Occur during Cr(VI) Biostimulation at the Hanford 100h Site, Based on Laboratory Experiments Described in the Supporting Information

transformation	geophysical attributes		
	seismic attributes	radar dielectric constant	electrical conductivity
pore water replacement by HRC	seismic attenuation increased significantly	decreased	increased significantly
pore water replacement by evolved gas bubbles	seismic velocities decreased slightly and seismic attenuation increased significantly	decreased	minor decrease
changes in solute concentration	negligible	negligible	decreased with decreasing TDS
change in volume or structure of solid phase	seismic attenuation and velocity increased as FeS precipitates formed	increased during calcite mass enrichment	decreased in response to formation of nonmetallic precipitates

of hydrological heterogeneity and hydrobiogeochemical transformations.

2.1. Laboratory Experiments. Geophysical monitoring of hydrobiogeochemical transformations is at a very early stage of development, and our understanding of geophysical responses to remediation end-products is still developing. As a step toward improving this understanding and to assist in the interpretation of the field-scale geophysical data sets, we performed a suite of laboratory experiments to explore how radar, seismic, and electrical signatures change during processes that were expected to be prevalent during the Cr(VI) biostimulation. Due to the recognized scaling and averaging challenges associated with applying laboratory-developed petrophysical relationships to field scale data sets and to uniqueness challenges that occur when multiple factors influence geophysical signatures (e.g., ref *3*), we did not develop petrophysical relationships at the laboratory scale and attempt to apply them to the field-scale monitoring data sets. Instead, we performed the laboratory experiments to gain insight about the relative sensitivities of the different geophysical attributes to transformational end-products; the insights were then used in the qualitative interpretation of the field-scale data sets.

The design of the laboratory experiments was based on the plausibility of detecting expected transformational end-products using particular geophysical methods and on the conceptual model of the biogeochemical reactions that were expected to occur during the Cr(VI) biostimulation (refer to the Supporting Information). Briefly, when HRC is injected into subsurface aquifers, hydrogen is produced via fermentation reactions associated with the polylactate decomposition. The produced hydrogen can decrease the pH in the vicinity of the injection well, which can facilitate dissolution of pH-sensitive minerals (such as calcites present in the Hanford sands). The produced hydrogen can facilitate microbial activity, which in turn can accelerate the sequential bioreduction of oxygen, nitrate, sulfate, and other competing electron acceptors. In the presence of Cr(VI), iron-containing minerals, and iron- and sulfate-reducing bacteria (all identified in the 100H Hanford formation), the decrease in redox potential can lead to the formation of insoluble Cr(III) precipitates. Calcite precipitates may also form, as the calcite dissolved near the injection well migrates downgradient and encounters more neutral pH groundwater. Other precipitates (such as FeS) also have the potential to form. The formation of gas bubbles and precipitates may reduce the porosity and permeability of the subsurface materials.

We chose to investigate the geophysical responses to four key transformations through a suite of laboratory experiments: (1) Pore-water replacement by the injected electron donor; (2) Gas bubble formation; (3) Variations in TDS; (4) Evolution, dissolution, or mineralogical alteration of solid phase constituents. The laboratory experiments are discussed in the Supporting Information, and the results are given in

Table 1. Relevant to the Cr(VI) biostimulation, the laboratory experiments revealed the following:

• Replacement of pore water by HRC dramatically increased seismic attenuation and electrical conductivity and slightly decreased dielectric constant.

• Gas generation associated with carbonate dissolution and denitrification processes decreased the dielectric constant and dramatically attenuated the seismic amplitudes.

• Changes in solute concentration or TDS (associated with processes such as sulfate reduction) directly correlated to changes in electrical conductivity.

• Evolution of disseminated minerals associated with reduction processes and calcite precipitation decreased the electrical conductivity, increased the seismic attenuation and velocity, and increased the dielectric constant.

Although not verified experimentally, if significant dissolution or precipitation occurs, the change in pore space could slightly alter the dielectric constant following eq 4.

2.2. Field Geochemical, Hydrological, and Geophysical Data Sets. *2.2.1. Field Geochemical Data Sets.* Aqueous and sediment field geochemical data sets were collected at the 100H site. Within the Hanford formation, groundwater samples were collected before, during, and after HRC injection from four discrete depths in both the injection well and the monitoring well. Groundwater sample analysis indicated approximate initial aqueous concentrations of nitrate (0.5 mM), iron oxides (233 mmol/kg), sulfate (0.7 mM), calcium (1.5 mM), magnesium (3.0 mM), and bicarbonate (1.5 mM). Limited sediment analysis was performed on 100H core samples obtained from the two additional wellbores that were drilled postinjection. Leached sediment calcium and carbonate concentrations were measured using the Hanford sand samples from both postinjection wells using the EPA 6010B and SM 2320B methods, respectively.

Groundwater analysis was performed over time using samples collected within the uppermost two sampling ports, which were both positioned within the Hanford formation. The upper port is located at a depth of 12.9 m (close to the groundwater surface) and the lower port is located at 14.1 m. The concentrations of combined organic acids (breakdown products of the HRC), nitrate and sulfate as a function of time were analyzed using a Dionex DX-120 ion chromatograph at LBNL. The $\delta^{13}C$ values of Dissolved Inorganic Carbon (DIC) in the samples were analyzed using procedures developed at the Center for Isotope Geochemistry at LBNL (*21*). The data are given as per mil deviations from the international standard, Vienna PeeDee Belemnite (VPDB), where $\delta^{13}C$ (‰) = $\{(^{13}C/^{12}C)_{sample}/(^{13}C/^{12}C)_{VPDB} - 1\} \times 1000$.

2.2.2. Field Hydrological Data Sets. Flowmeter logs were collected in the saturated sections of Wells 44 and 45 by Quantum Engineering Corporation (QEC) using a one-foot sampling interval. Pump test data were used to reduce the flowmeter measurements in terms of 1-D variations in

hydraulic conductivity at the wellbore locations following developed procedures (22).

2.2.3. Field Geophysical Data Sets. Tomographic radar (100 MHz) and seismic (1000–7000 Hz) data sets were collected between the injection and monitoring boreholes at the 100H site during thirteen acquisition campaigns and over the course of ~3 years. The Supporting Information provides a time table associated with the field geophysical and pumping campaigns; details associated with the geophysical data acquisition and inversion procedures; examples of raw and inverted geophysical data sets; procedures for estimating changes in geophysical attributes; and a discussion of the impact of acquisition geometry and inversion procedure on the estimated geophysical attributes.

The geophysical "baseline" tomograms were first used with the field flowmeter and pump test data to estimate hydrological zonation. The time-lapse geophysical data sets were then used in conjunction with the baseline data sets to detect changes in dielectric constant, electrical conductivity, and seismic attenuation that occurred over time during the manipulation experiment. Assessing the geophysical measurements or attributes in a "time-lapse" mode provides a particularly powerful approach for monitoring small changes in natural systems (e.g., ref 3).

3. Interpretation and Discussion

3.1. Field Geochemical Data Sets. The concentrations of Cr(VI), organic acids, $\delta^{13}C$, nitrate, and sulfate over a two year time frame following HRC injection are shown in Figure 1. Figures 1a and b reveal that the Cr(VI) concentration in both wells initially decreased significantly and remained depressed relative to background conditions over time. Concentrations in the samples collected from the shallower port, located directly beneath the water table, rebounded toward background conditions, while concentrations associated with the deeper port stayed below MCL for the duration of the two year monitoring period.

Figure 1c shows that the concentration of organic acids in both intervals in the injection well started very high, dropped down initially, and then rebounded by the end of the first pumping campaign. After pumping stopped, the organic acid concentrations decreased slowly with time in both intervals, reaching background in the upper interval about 450 days after injection. In the monitoring well, the organic acids initially increased above background at 15 days (Figure 1d). After the pumping stopped, the organic acid concentrations dropped to background and remained there until the second pumping campaign when they rebounded in both intervals. At the end of the second pumping campaign, the concentrations dropped back down to background levels.

Figure 1e shows that the $\delta^{13}C$ of the DIC in the injection well was significantly elevated at both depths during the first pumping campaign, indicating that the inorganic carbon in the groundwater was primarily derived from the labeled HRC. After pumping stopped, the $\delta^{13}C$ of the DIC dropped down to close to background ($-15‰$) after approximately one month. This could be an indication that microbial activity was diminished or that aerobic metabolism had become limited by the reduced dissolved oxygen content of the groundwater in the vicinity of the injection well. With time, $\delta^{13}C$ began to increase slowly until the beginning of the second pumping campaign when it increased. When the second pumping campaign ended, the $\delta^{13}C$ of the DIC dropped down again, but remain higher than it had been after the first pumping campaign. In the monitoring well, the $\delta^{13}C$ of the DIC tracked the organic acid content of the groundwater (Figure 1f). In the deeper interval, the $\delta^{13}C$ of the DIC increased to $>30‰$ during the first pumping campaign. This is considerably higher than the isotopic composition of the HRC with the ^{13}C-labeled lactate (15‰),

suggesting preferential transport and degradation of the lactate versus the HRC.

Nitrate concentration in the injection well is plotted in Figure 1g. In the upper sampling interval the concentrations started out above background due to nitrate added with the HRC, but quickly dropped to zero and remained depressed throughout the test. In the deeper interval, nitrate had already disappeared by the time the first sample was taken and remained at zero throughout the experiment. In the monitoring well (Figure 1h), the nitrate concentrations in both intervals decreased to zero with the arrival of the organic acids during the first pumping campaign. After the pumping stopped, nitrate slowly rebounded, reaching background after approximately two months. This pattern was repeated during the second pumping campaign. During the third pumping campaign, nitrate in the lower interval dropped to zero, but only decreased briefly to about half of background in the upper interval.

In both sampling intervals in the injection well, sulfate remained near background concentrations throughout the initial pumping campaign (Figure 1i). When the pumping stopped, the sulfate concentrations decreased, reaching <5 ppm in the lower interval within a month and in the upper interval after about 6 months. During the second pumping campaign, the concentrations increased in both intervals, but dropped back down when pumping stopped. After approximately one month, the concentrations began to increase. For the third pumping campaign there is only data for the upper interval. In that interval, the sulfate concentration initially dropped slightly but then rebounded to background after a couple of weeks. The sulfate in both intervals of the monitoring well (Figure 1j) dropped slightly during the first pumping campaign but rebounded as soon as the pumping stopped. During the second pumping campaign there were more significant decreases in sulfate in both intervals, with the upper level dropping below 30 ppm and the lower level to less than 5 ppm. After the pumping stopped, the sulfate concentrations in both intervals returned to background levels. Interestingly, with time the sulfate concentrations increased above background levels, especially in the lower interval, possibly representing reoxidation of precipitated sulfides.

The geochemical data shown in Figure 1 suggest that the microbial community was stimulated by injection of HRC, rapidly depleting the available oxygen, reducing nitrate and sulfate, and decreasing the concentration of Cr(VI). These effects happened within the first 15 days postinjection, and were more pronounced and sustained in the injection well. The rebound in sulfate during pumping is interpreted to be the result of up-gradient water with higher redox potential being pulled into the vicinity of the injection well. In both intervals in the down gradient monitoring well, nitrate concentrations decreased to near zero during the pumping campaigns (coincident with the arrival of organic acids) and then slowly rebounded after the pumping stopped. Sulfate only decreased slightly during the first pumping campaign, but dropped more significantly during the second campaign, especially in the deeper interval. This pattern of chemical change is consistent with decreasing redox potential due to microbial degradation of the HRC and its byproducts when the pumping was drawing the organic acids into the vicinity of the borehole.

Sediment analysis of Hanford sand core samples collected from the postinjection wells suggests that the concentrations of leached carbonate and calcium in the well located between the injection and monitoring well were 50 and 11% greater, respectively, than concentrations associated with the well located outside of the treatment region. This analysis suggested that a mass enrichment of calcite likely occurred downgradient from the HRC injection well relative to
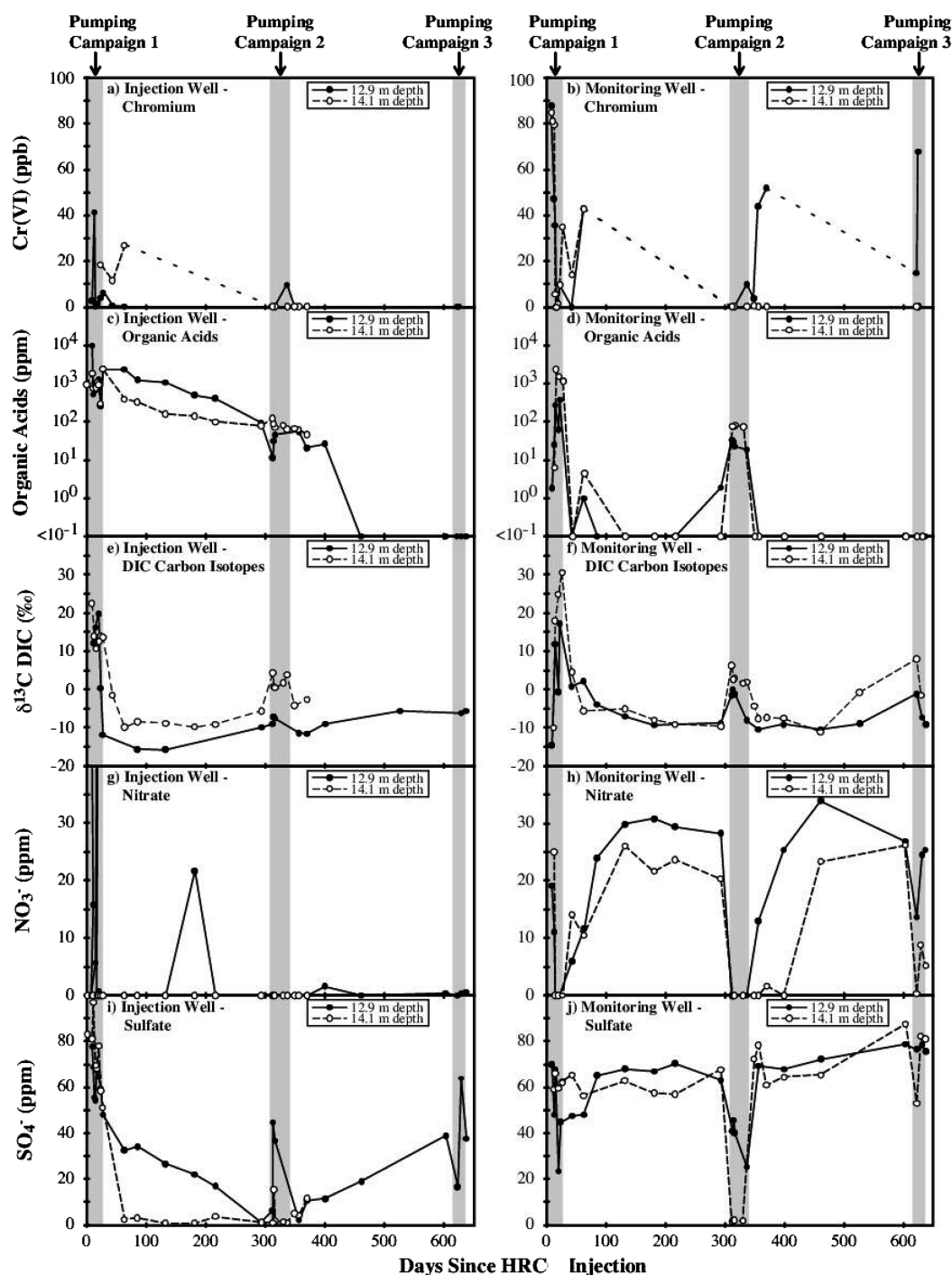
FIGURE 1. Results of geochemical analysis of groundwater samples collected over time using the shallow and deep sampling ports within the Hanford formation at both the injection (left column) and monitoring (right column) wells, including (a and b) Cr(VI) concentration; (c and d) organic acids; (e and f) $\delta^{13}C$ values of DIC; (g and h) nitrate concentration; and (i and j) sulfate. The vertical shaded regions indicate time periods associated with three different pumping campaigns.

preinjection conditions. This observation is consistent with our conceptual model, which suggests that injection of HRC could dissolve calcites in the vicinity of the injection well, which could subsequently precipitate downgradient upon encountering more neutral pH groundwater.

3.2. Hydrological Zonation. The baseline tomographic data sets were used together with electromagnetic flowmeter data and pump test data to estimate the hydrological zonation within the Hanford formation target zone. The reduced flowmeter measurements in the Hanford formation revealed that the hydraulic conductivity was bimodally distributed, suggesting that it would be most reasonable to estimate the distribution of higher and lower hydraulic conductivity zones

in the Hanford formation, or hydrological zonation. To perform the estimation, we used an indicator approach and a linear discriminant analysis technique (23), which is a technique for categorizing a set of observations into several predefined classes. We divided the hydraulic conductivity into two classes: a class representing all values lower than a cutoff value of 10^{-3} cm/s, which was the median hydraulic conductivity value (i.e., indicator = 0), and another class representing all values higher than the cutoff value (i.e., indicator = 1). The mean log hydraulic conductivity values of the two categories were −3.47 and −2.33 cm/s, respectively, and the corresponding within-group standard deviations

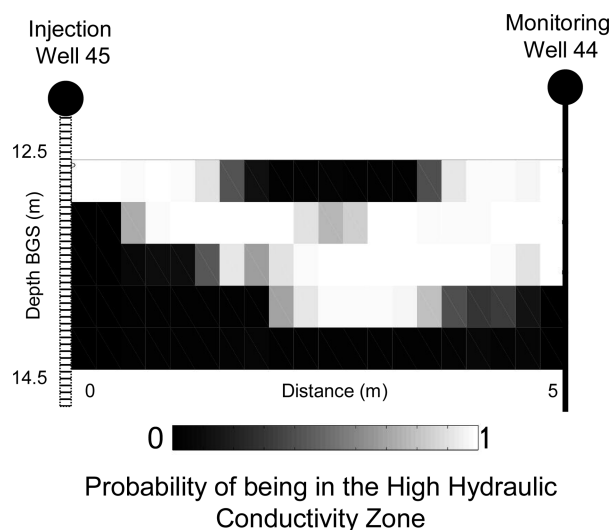Probability of being in the High Hydraulic
Conductivity Zone

FIGURE 2. Probability of being in a high hydraulic conductivity zone within the Hanford formation, as estimated using baseline tomographic data sets, flowmeter and slug test data, and a linear discriminant approach. The figure suggests that the probability of hydraulic conductivity being higher than the median flowmeter value is greater in the upper part than in the lower part of the sandy Hanford formation.

were lower than the overall standard deviation of the hydraulic conductivity data set.

Using the linear discriminant approach, the defined cutoff value, and the tomographic data, we obtained the spatial distribution of the probability being in the higher hydraulic conductivity zone of the Hanford formation (Figure 2). Although the flowmeter data in the Hanford formation are quite sparse and the acquisition geometry and inversion approach impact the baseline geophysical images used for this interpretation, Figure 2 generally suggests that the probability of the hydraulic conductivity being higher than the median value is greater in the upper part of the sandy Hanford formation than the lower part.

3.3. Integrated Interpretation of Geophysical Monitoring Data. Figure 3 illustrates contoured changes in estimated dielectric constant, electrical conductivity, and seismic attenuation in the saturated Hanford formation relative to the baseline data set values over a three year monitoring time frame. The subset of the time-lapse images shown is representative of the entire geophysical monitoring data set. In general, Figure 3 illustrates that the changes in dielectric constant and electrical conductivity occurred progressively over time. In contrast, the seismic attenuation difference images reveal a complete loss of signal in portions of the Hanford formation as early as one day after injection of HRC, which was sustained throughout the monitoring period.

Below, we provide an interpretation of the field-scale geophysical data sets in terms of four key processes: distribution of the injected electron donor; evolution of gas bubbles; changes in TDS; and solid phase transformations. The interpretation of the time-lapse geophysical data sets is qualitative in nature and was developed to jointly honor our conceptual model, the indications of geophysical responses provided from laboratory-scale experiments (Table 1), and our interpretation of field-scale geochemical data sets.

3.3.1. Electron Donor Distribution. Figure 3 shows that by 1 day after HRC injection, the estimated electrical conductivity dramatically increased, the seismic signal was completely attenuated, and the dielectric constant was reduced near the injection zone relative to baseline conditions. At 1 day after injection, the zone of increased electrical conductivity extended from the injection well toward well 44, both horizontally along the Hanford–Ringold interface,

and diagonally from the bottom of Well 45 toward the pump (located just beneath the water table in Well 44). Of interest is the development by day 3 postinjection of a wedge-shaped zone of dramatically increased electrical conductivity and attenuated seismic energy. Because the observed changes are consistent with the laboratory responses of pore water replacement by HRC (Table 1), we interpret the responses within the wedge-shaped region to be associated with the emplacement and distribution of the organic amendment in the 100H subsurface. The wedge region appears to intersect the monitoring well by day 13, which is consistent with the increase in organic acids at the monitoring well that was detected by day 15 postinjection (Figure 1).

Comparison of these difference images with the hydraulic conductivity zonation estimates (Figure 2) suggests that although the entire saturated section of the injection well was screened, the HRC appears to have rapidly sunk through the well and to have entered the system at the base of the Hanford formation. The HRC then appears to have been preferentially pulled upward during pumping into the higher conductivity zone (Figure 2) as well as horizontally along the Hanford–Ringold formation interface toward Well 44. This result demonstrates the influence of hydrogeological heterogeneity on electron donor distribution at the 100H site.

3.3.2. Evolution of Gas Bubbles. Based on our conceptual model and laboratory experimental results, we expected gas to be generated near the injection well due to both CO_2 dissolution and denitrification processes. Although the laboratory studies suggested that seismic amplitudes are extremely sensitive to the presence of small volumes of gas bubbles (Table 1), it was impossible to use these data to interpret subsequent bubble formation within the wedge-shaped area because much of the seismic data had been attenuated by the first day postinjection. As such, we rely here only on indications provided by the radar data sets. As shown by Figure 3, the early time dielectric constant values did not continue to decrease after HRC was injected. This observation suggests that if gas bubbles are being generated near the injection well, their volume is small, since the impact on the dielectric constant appears to be negligible relative to the impact of other processes. Because field gas monitoring was not performed during the experiment, the interpretation of gas bubble production is based on geophysical data alone.

3.3.3. TDS. Figure 3 suggests that the elevated electrical conductivity associated with the wedge-shaped region persisted only for several days. However, the wedge-shaped region was still discernible throughout much of the experiment, as the electrical conductivity values around and downgradient of the wedge decreased over time, and the dielectric constant values within the wedge-shaped area increased. We designate the region surrounding the wedge as the "reaction halo" and interpret here the change in electrical conductivity within the halo that surrounds the wedge.

The laboratory experiments suggest that a decrease in TDS should significantly decrease the electrical conductivity (Table 1). Figure 3 illustrates that the electrical conductivity decreased significantly in the reaction halo region at 30 days after injection, recovered toward background electrical conductivity values at 86 days after injection, and then decreased again within the reaction halo at 324 days after injection. Comparison with the monitoring well geochemical data (Figure 1) suggests that the variations in electrical conductivity values in the reaction halo area over time corresponded with sulfate and nitrate concentrations: the electrical conductivity decreased most significantly during pumping (when sulfate and nitrate were most reduced), and increased when pumping stopped (as nitrate and sulfate concentrations rebounded toward background levels). Al-
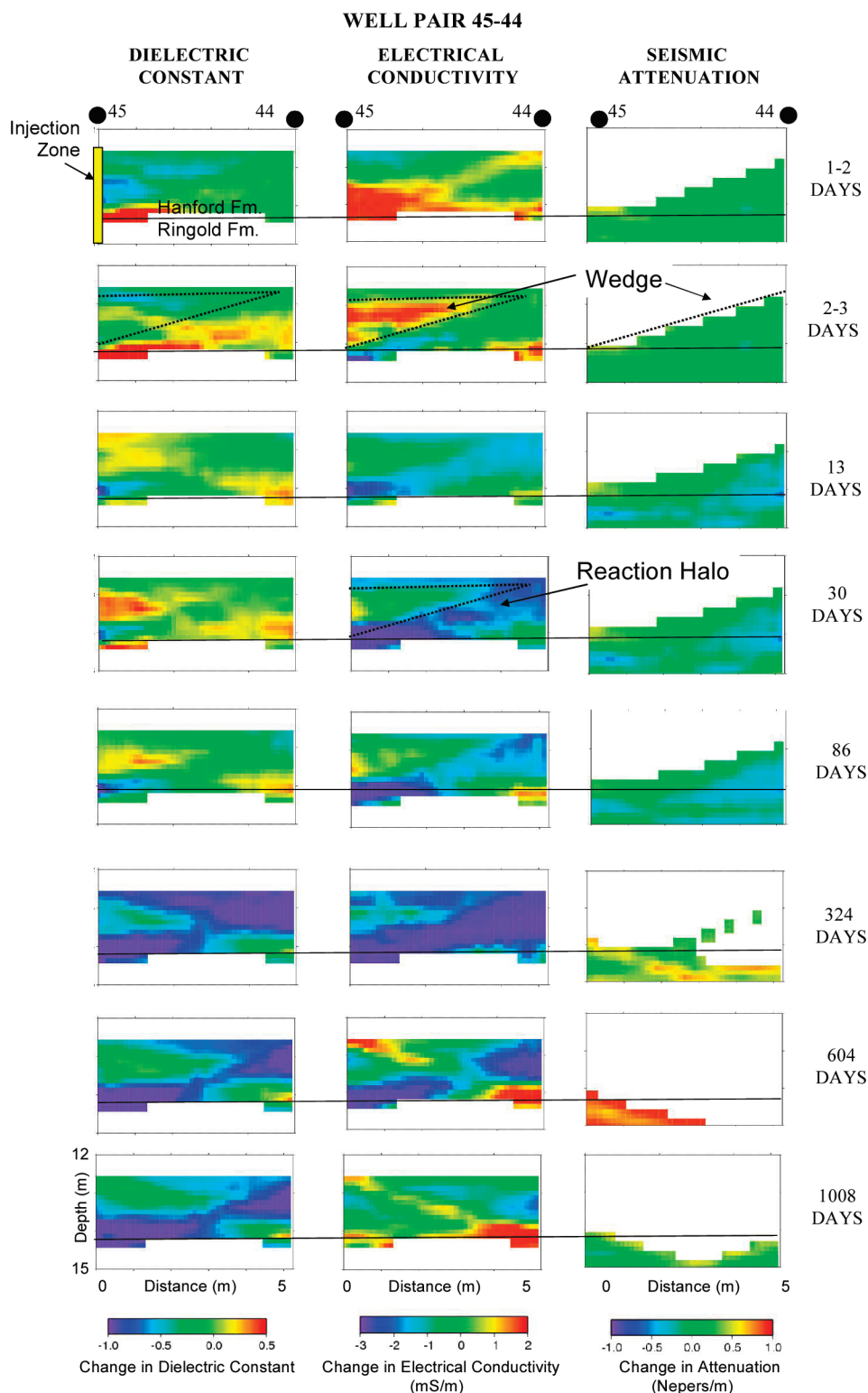
WELL PAIR 45-44

FIGURE 3. Changes in estimated geophysical attributes relative to baseline values within the saturated Hanford stimulation zone and on selected days after HRC injection. These images were used in conjunction with biogeophysical laboratory experimental results and field geochemical data to interpret the spatiotemporal distribution of hydrobiogeochemical processes associated with the Cr(VI) biostimulation at the 100H site.

though not measured, manganese production associated with Cr(VI) reduction may also contribute to TDS variations.

We interpret the changes in electrical conductivity in the reaction halo to be due to changes in TDS, which fluctuate as a function of pumping activity. To test this hypothesis, the electrical conductivity estimates associated with tomographic pixels adjacent to the shallow, downgradient sampling port were averaged and used with eqs 1 and 2 to estimate changes

in TDS. The favorable comparison (shown in the Supporting Information) suggests that the electrical conductivity variations that occurred between the first and second pumping campaigns responded primarily to changes in TDS.

3.3.4. Solid Phase Transformations. Our conceptual model and laboratory experiments suggests that several solid phase transformations could occur during biostimulation with HRC, including the dissolution of calcite upon amendment injec-

tion and the subsequent formation of disseminated minerals, such as FeS. Relationships such as eqs 1 and 4 further indicate that porosity changes, potentially caused by the formation and dissolution of minerals, can in turn alter the geophysical attributes.

Figure 3 illustrates that after introduction of the HRC, the dielectric constant increased in the plume injection area relative to baseline. This increase was first evident at 30 days post injection and continued to 302 days post injection. After this time, the dielectric constant decreased in the reaction halo region relative to baseline by ~7%. By 310 days postinjection, the electrical conductivity in the reaction halo decreased more substantially and sustainably than previous decreases.

Using the mixing model provided by eq 4, we interpret the radar changes to be due to an early time increase in porosity near the injection well (as HRC dissolved calcites in the Hanford sands), followed by a decrease in porosity during later times downgradient as calcites precipitated upon encountering more neutral pH regions. The decrease in electrical conductivity, which is exemplified by the 324 days post injection tomogram in Figure 3, is similar in magnitude to the decreases in electrical conductivity detected at the laboratory scale during the formation of finely disseminated precipitates (such as FeS). Although time-lapse porosity and detailed mineralogical data were not collected during the field experiment to validate this interpretation, the interpretation of downgradient calcite precipitation is supported by the sediment geochemistry data, which revealed a mass enrichment of calcium and carbonate along the experimental centerline relative to regions outside of the stimulation region.

3.4. Discussion. In Section 3.3, we interpreted the monitoring data set in terms of specific processes. Because the monitoring data were collected to provide information about system dynamics over space and time in response to the HRC injection, below we summarize the integrated interpretation of the geophysical monitoring data in terms of early, intermediate, and late experimental stage transformations.

3.4.1. Early Stage Transformations (≤ 3 days). Immediately following the HRC injection, the field geophysical difference tomograms revealed a severe attenuation of seismic amplitude, an increase in electrical conductivity and a decrease in dielectric constant near the injection well. Consistent with the laboratory signatures of pore water replacement by HRC, we interpret the early stage of the field experiment to be dominated by the introduction of HRC into the Hanford formation. Comparison of the interpretation of the HRC distribution with the hydraulic conductivity zonation estimates suggests that heterogeneity governed the early emplacement of HRC within the higher hydraulic conductivity zone and along the Hanford−Ringold interface.

3.4.2. Intermediate Stage Transformations (~13–302 days). Several processes are interpreted to be associated with the intermediate stage of the experiment: injectate migration, calcite dissolution near the injection well, and changes in TDS associated with pumping. By 15 days post injection, both the geophysical and aqueous geochemical data suggested that the HRC and/or its breakdown products had migrated to the downgradient well. The dielectric increase observed near the injection well during the early part of the intermediate stage are interpreted to be due to an increase in porosity associated with the dissolution of calcite by the acidic HRC injectate. The wellbore geochemical data suggested that nitrate and sulfate concentrations fluctuated as aquifer redox conditions changed due to pumping. Illustrating the benefit of geophysical monitoring, the electrical conductivity difference tomograms revealed corresponding spatiotemporal variations of these interpreted

TDS fluctuations along the two-dimensional transect that connected the injection and monitoring well.

3.4.3. Late Stage Transformations (302–604 days). Processes occurring during the late experimental times are interpreted to be dominated by solid-phase transformations. The decrease in electrical conductivity (beyond what is expected based on decreases in TDS), decrease in dielectric constant, and further decrease in seismic attenuation is interpreted to be due to the formation of disseminated precipitates and associated porosity reduction within the reaction halo. Calcites, which were interpreted to have been dissolved upon HRC injection, are interpreted to have precipitated upon encountering more neutral pH groundwater downgradient. This interpretation is consistent with the sediment geochemical data that were collected postinjection, which revealed higher calcite and carbonate concentrations than concentrations associated with core samples located outside of the stimulated zone. Although other minerals (such as FeS) may also have formed and contributed to the observed geophysical response and interpreted porosity reduction, detailed time-lapse porosity and sediment iron geochemical data are not available for corroboration.

3.4.4. Very Late Stage Transformations (1008 days). Because wellbore geochemical data are only available for two years following the HRC injection, only the geophysical data sets are available for interpreting the very late stage transformations. This data set revealed that by three years post injection, the electrical conductivity had rebounded, the seismic signal was attenuated, and the dielectric constant values were depressed in the reaction halo relative to baseline conditions. Following the interpretations presented previously and consistent with our conceptual model and laboratory experiments, these geophysical responses suggest that TDS rebounded to background levels and that the interpreted porosity reduction due to the formation of precipitates continued to impact the system ~3 years post injection.

The integrated interpretation illustrates the potential benefit of using time-lapse geophysical data sets to interpret biogeochemical transformations associated with a bioremediation treatment in high resolution, over field relevant scales, and in a minimally invasive manner. We found that multiple types of geophysical measurements, collected over a long time period, revealed small but spatially persistent changes in geophysical attributes that were consistent with our conceptual model, laboratory experimental results, and field geochemical data sets. In addition to illustrating the potential of geophysical data sets for remote monitoring of field-scale processes, our study also illustrated the influence of pumping and heterogeneity on the transformations. Although these impacts are not unexpected, it is rare in practice to have both high enough characterization and monitoring data to be able to explore the influence of heterogeneity on biogeochemical transformations at the field scale.

Although the potential benefits of using integrated time-lapse, field-scale data sets for monitoring biogeochemical transformations are evident, there are currently several uncertainties associated with the approach and the interpretation provided herein. For example, although field-scale aqueous and limited sedimentary data were available to corroborate some of the interpreted processes (such as HRC distribution, changes in TDS, mass enrichment in calcite), time-lapse field measurements of gas bubble evolution, mineralogy, and porosity would have been helpful for corroborating the geophysical interpretation of other processes.

There are also several challenges and limitations associated with using extensive yet indirect geophysical data sets to interpret hydrobiogeochemical processes, including those associated with scale, uniqueness, petrophysics, estimation,

and imaging (e.g., ref 3). Although our laboratory and field-scale geophysical responses to particular processes were generally very consistent, this consistency may not be realized under different conditions. As is further discussed in the Supporting Information and in agreement with previous studies (e.g., ref 24) both tomographic data acquisition and inversion procedures impact the image of the geophysical attributes that were interpreted for this study. With this uncertainty, the images were generally not used to estimate biogeochemical property values or precise boundaries of regions undergoing particular transformations. Instead, the time-lapse geophysical attributes were used to define regions where transformations occurred and to indicate possible end-products associated with the transformations.

This study illustrates the wealth of information that geophysical data sets have the potential to provide about variations in biogeochemical processes associated with Cr(VI) biostimulation; the integrated approach led to an interpretation that would have been difficult to extract from wellbore geochemical data alone. Time-lapse geophysical data sets can also potentially be used to monitor other remediation treatments besides biostimulation using HRC. Other reasonable geophysical imaging targets include monitoring the distribution and reaction products associated with other viscous amendments (such as vegetable oil or molasses), mobile and soluble electron donors (such as lactate, acetate, ethanol, and other organic compounds), or solid particles (such as nanoscale iron), as well as associated hydrological−biogeochemical transformations. With the continuing hydrogeophysical and biogeophysical research that is currently underway within the community, we expect that the use of geophysical methods for exploring complex and coupled hydrobiogeochemical subsurface processes associated with remedial treatments to increase in frequency and to become more quantitative in nature. Once developed, such geophysical approaches could conceivably be used in a semi-autonomous and long-term monitoring mode. Although more research is needed before these methods can be considered as routine remediation monitoring tools, this study indicates that it is an avenue worthy of further pursuit.

Acknowledgments

Supporting Information Available

Additional details about this study are provided in the Supporting Information about the: Hanford Study Site, biostimulation experiment; biogeochemical conceptual model; laboratory biogeophysical experiments; acquisition and inversion of field geophysical data sets; and assessment of the quality and use of geophysical data for monitoring transformations associated with the biostimulation. This material is available free of charge via the Internet at http://pubs.acs.org.

Literature Cited

(1) Rubin, Y.; Hubbard, S. *Hydrogeophysics*; Springer: The Netherlands, 2005; p 523.

(2) Vereecken, H.; Binley, A.; Cassiani, G.; Revil, A.; Titov, K. *Applied Hydrogeophysics*; Springer: The Netherlands, 2006; p 383.

(3) Hubbard, S. S.; Rubin, Y. Introduction to Hydrogeophysics, Chapter 1. In *Hydrogeophysics*; Rubin, Y., Hubbard, S., Eds.; Springer: The Netherlands, 2005; pp 3–21.

(4) Scheibe, T. S.; Chien, Y. J. An evaluation of conditioning data for solute transport prediction. *Ground Water* **2003**, *41* (2), 128–141.

(5) Scheibe, T.; Fang, Y.; Murray, C. J.; Roden, E. E.; Chen, J.; Chien, Y.; Brooks, S. C.; Hubbard, S. S. Transport and biogeochemical reactions of metals in a physically and chemically heterogeneous aquifer. *Geosphere* **2006**, *2* 4, 220−235, DOI: 10.1130/GES00029.1.

(6) Atekwana, E. A.; Werkema, D. D.; Atekwana, E. A. Biogeophysics: The effects of microbial processes on geophysical properties of the shallow subsurface, Chapter 6. In *Applied Hydrogeophysics*; Vereecken, H., Binley, A., Cassiani, G., Revil, A., Titov, K. Eds.; Springer: The Netherlands, 2006; pp 161–193.

(7) Williams, K. H.; Ntarlagiannis, D.; Slater, L. D.; Dohnalkova, A.; Hubbard, S. S.; Banfield, J. F. Geophysical imaging of stimulated microbial biomineralization. *Environ. Sci. Technol.* **2005**, *39* (19), 7592−7600, DOI: 10.1021/es0504035.

(8) Lane, J. W.; Day-Lewis, F. D.; Casey, C. C. Geophysical monitoring of a field-scale biostimulation pilot project. *Ground Water* **2006**, *443*, 430−443, DOI: 10.1111/j.1745-6584.2005.00134.

(9) Archie, G. E. The electrical resistivity log as an aid in determining some reservoir characteristics. *Trans. Amer. Inst. Min. Metall. Pet. Eng.* **1942**, *146*, 54–62.

(10) Fishman, M. J.; Friedman, L. C. *Methods of determination of organic substances and fluvial sediments, Techniques of Water Resource Investigations of the U.S. Geological Survey, Book 5, Chapter A1*; U.S Geological Survey: Reston, VA, 1989.

(11) Binley, A.; Kemna, A. DC resistivity and induced polarization methods, Chapter 5. In *Hydrogeophysics*; Rubin, Y., Hubbard, S., Eds.; Springer: The Netherlands, 2005; pp 129–156.

(12) Lesmes, D.; Friedman, S. Electrical and hydrological properties, Chapter 4. In *Hydrogeophysics*; Rubin, Y., Hubbard, S., Eds.; Springer: The Netherlands, 2005; pp 87–128.

(13) Topp, C. G.; Davis, J. L.; Annan, A. P. Electromagnetic determination of soil water content: measurements in coaxial transmission lines. *Water Resour. Res.* **1980**, *16* (3), 574–582.

(14) Peterson, J. E. Pre-inversion processing and analysis of tomographic radar data. *J. Environ. Eng. Geophys.* **2001**, *6* (1), 1–18.

(15) Davis, J. L.; Annan, A. P. Ground penetrating radar for high resolution mapping of soil and rock stratigraphy. *Geophys. Prospect.* **1989**, *37* (5), 531–551.

(16) Wharton, R. P.; Hazen, G. A.; Rau, R. N.; Best, D. L. Electromagnetic propagation logging-Advances in technique and interpretation, Society of Petroleum Engineers Paper, **1980**, *9267*, 12.

(17) Chang, P. D.; Alumbaugh, D.; Brainard, J.; Hall, L. Cross-borehole ground penetrating radar for monitoring and imaging solute transport within the vadose zone *Water Resour. Res.* **2006**, *42*, DOI: 10.1029/2004WR003871.

(18) Dalton, F. N.; Herkelrath, W. N.; Rawlins, D. S.; Rhoades, J. D. Time-domain reflectometry: Simultaneous measurement of soil water content and electrical conductivity with a single probe. *Science* **1984**, *224* (4652), 989–990.

(19) Steeples, D. W. Shallow seismic methods, Chapter 8. In *Hydrogeophysics*; Rubin, Y., Hubbard, S. S., Eds.; Springer: The Netherlands, 2005.

(20) Pride, S. Relationships between seismic and hydrological properties, Chapter 9. In *Hydrogeophysics*; Rubin, Y., Hubbard, S. S., Eds.; Springer: The Netherlands, 2005; pp 253–290.

(21) Torn, M.; Davis, S.; Bird, J. A.; Shaw, M. R.; Conrad, M. E. Automated analysis of $^{13}C/^{12}C$ ratios in dissolved CO_2 and dissolved inorganic carbon for ecological and environmental applications. *Rapid Commun. Mass Spectrom.* **2003**, *17* (23), 2675–2682.

(22) Molz, F. J.; Boman, G. K.; Young, S. C.; Waldrop, W. R. Borehole flowmeters: Field applications and data analysis. *J. Hydrol.* **1994**, *163*, 347–371.

(23) Venables, W. N.; Ripley, B. D. *Modern Applied Statistics with S-Plus*; Springer: New York, 1999.

(24) Day-Lewis, F. D.; Lane, J. W. Assessing the resolution-dependent utility of tomograms for geostatistics. *Geophys. Res. Lett.* **2004**, *31*, L07503 DOI:10.1029/2004GL019617.

ES071702S